Nostalgin: Extracting 3D City Models from Historical Image Data

Amol Kapoor[*]
ajkapoor@google.com
Google Research
New York, NY

Hunter Larco[*]
hunterlarco@google.com
Google Research
New York, NY

Raimondas Kiveris
rkiveris@google.com
Google Research
New York, NY

ABSTRACT

What did it feel like to walk through a city from the past? In this work, we describe Nostalgin (Nostalgia Engine), a method that can faithfully reconstruct cities from historical images. Unlike existing work in city reconstruction, we focus on the task of reconstructing 3D cities from historical images. Working with historical image data is substantially more difficult, as there are significantly fewer buildings available and the details of the camera parameters which captured the images are unknown. Nostalgin can generate a city model even if there is only a single image per facade, regardless of viewpoint or occlusions. To achieve this, our novel architecture combines image segmentation, rectification, and inpainting. We motivate our design decisions with experimental analysis of individual components of our pipeline, and show that we can improve on baselines in both speed and visual realism. We demonstrate the efficacy of our pipeline by recreating two 1940s Manhattan city blocks. We aim to deploy Nostalgin as an open source platform where users can generate immersive historical experiences from their own photos.

CCS CONCEPTS

• **Applied computing** → **Architecture (buildings)**; **Computer-aided design**; • **Computing methodologies** → *Machine learning*; *Shape modeling*; • **Human-centered computing** → Human computer interaction (HCI).

KEYWORDS

3D modeling, computer vision, city generation, neural networks

ACM Reference Format:
Amol Kapoor, Hunter Larco, and Raimondas Kiveris. 2019. Nostalgin: Extracting 3D City Models from Historical Image Data. In *KDD '19: ACM SIGKDD Conference on Knowledge Discovery and Data Mining, August 04–08, 2019, Anchorage, AK*. ACM, New York, NY, USA, 9 pages. https://doi.org/10.1145/1122445.1122456

Figure 1: A 3D reconstruction of the NE Corner of 9th Avenue, 16th Street, New York, NY as it looked in the 1940s.

1 INTRODUCTION

There is significant interest in the automatic generation of 3D city models. Such models are used in Google Maps and Google Earth, in popular video games, in urban planning simulations, and more. However, these models are prohibitively expensive to create. Traditionally, large studios spend thousands of dollars and man-hours to create realistic worlds. Commercial procedural modeling engines are a powerful tool to address some of these issues, but they are limited in their accuracy and require significant manual effort to fine tune.

There is also significant interest in historical image data. Individuals are fascinated with historical data as a means of capturing nostalgia, pursuing education, connecting with family and elders, or preserving culture. Individuals are especially excited about historical data that allows them to interact with bygone eras, experiencing settings and environments that no longer exist. We note that city photography is a natural source of realistic detail, and that there is a significant wealth of historical and modern city imagery. With this in mind, we are interested in the problem of automatically generating city models from historical images of cities to expose historical data to users through an immersive walkthrough experience.

Historical images are difficult to access and even more so to utilize, especially in comparison to modern image and video data. Historical images are inherently more sparse than modern images, in that there are simply fewer available. Thus, when working with historical data, it is difficult to create large datasets with specific requirements, such as all images being occlusion-free, or taken from the same camera angle. It is also difficult to find multiple historical images of the same subject. Finally, historical metadata is nonexistent. Unlike modern images, which often come with EXIF information like geolocation and camera intrinsics, historical data often only includes raw pixel information.

Recent advances in computer vision have enabled the automatic recovery and extraction of missing information from images. Computers have gained the ability to semantically parse [8], rectify [28], and inpaint [26] images, and extract 3D scene understanding [19] from images. Research has been done to extract city geometries from images as well [18]. Though these advances in computer vision are powerful, they often come with caveats and assumptions that make broad usage difficult. Many approaches require intrinsic

[*]Both authors contributed equally to this research.

KDD '19, August 04–08, 2019, Anchorage, AK

ACM ISBN 978-1-4503-9999-9/18/06…$15.00
https://doi.org/10.1145/1122445.1122456

or extrinsic camera parameters like focal length or relative geolocation; others are limited to toy datasets or require multiple input images; others still require fairly significant human intervention. These limitations carry over to 3D city generators. For example, the work of [19] requires a color image with few occlusions and a user-generated trace of the building model to create a single building. These limitations are not scalable and are unsuited for historical data, which is sparse and has few image guarantees.

In this work, we describe a scalable, modular 3D city generation pipeline named Nostalgin (Nostalgia Engine) that leverages, combines, and builds on advances in computer vision. Nostalgin is designed to uniquely handle the difficulties that arise when dealing with historical image data. Our novel contributions are as follows:

(1) a combined deep and algorithmic approach to image segmentation that produces extremely tight segmentation masks;
(2) a novel approach to image rectification that can uniquely handle historical image data;
(3) a method for efficient deep image inpainting on extremely large images;
(4) a modeling system to place rectified facade images into a 3D world.

For each section, we motivate our design choices and provide experimental analysis demonstrating the qualitative and quantitative efficacy of each component. We also analyze our overarching design and discuss approaches for better run-time and memory cost. Finally, we present two reconstructed blocks of Manhattan that are automatically generated using images taken from historical datasets of New York City in the 1940s.

2 RELATED WORK

For non-deep-learning related work, we refer primarily to the review in [18], which describes many important methods for accurate modeling 3D cities. These approaches can broadly be split by the type and amount of ingested data. Early approaches focus on street-level image data as an obvious source of information. Several works extract 3D geometry using multi-view image reconstruction [1, 2, 10], which often relies on understanding the general location of an image in order to make sense of the contents. These works contrast to single-view reconstruction, which use heuristics such as general shape and symmetry to mimic real world constructs [11, 14, 15], or are highly interactive and require user input [9, 11, 20]. More recently, development of hardware has made aerial imagery, satellite imagery, and LIDAR mapping significantly more viable. These forms of data allow for new kinds of 3D reconstruction. For example, [12] proposes a method of combining street-level imagery, GIS footprints, and polygonal meshes (processed aerial images) to extract models, while [13] proposes utilizing aerial urban LIDAR scans. For completeness, we note that procedural modeling [22] and manual modeling [25] are popular and well utilized in many practical applications.

Due to the recent popularity of deep learning, a number of publications have proposed deep models to learn automatic reconstruction. Recent work has improved on extracting intrinsic camera parameters and object poses [7], semantically parsing facades [17], or combining machine learning techniques with procedural grammars for reconstruction [19]. We note that many approaches to deep 3D reconstruction are not scalable and are very difficult to train outside of academic datasets (e.g. ShapeNet [5] which consists of low poly or voxel models that are not suitable for a city reconstruction task).

In dealing primarily with historical data, we tackle a different task than many of the above methods. We cannot rely on any guarantees regarding multiple views, and do not have access to tools such as LIDAR, aerial data, satellites, or even cameras that measure parameters like focal length and position. We aim for a high degree of accuracy, potentially at the expense of detailed 3D features. Finally, we desire a system that minimizes human input in order to generate entire cities at scale.

3 PROPOSED METHOD

In this section, we describe the design of Nostalgin. We identify four key tasks in our image-to-model conversion process: image parsing, viewpoint normalization, occlusion removal, and 3D conversion. For each section, we provide a description of the sub-problem, our requirements for the solution, and the design of our final component. Experiments motivating our design choices are in Section 4.

3.1 Generalizations and Assumptions

Because we are working with historical image data, we try to minimize the number of requirements related to the contents of the image and the metadata available. To that end, we design Nostalgin to be as general as possible without relying on anything other than the raw image data. At the same time, we purposely design our pipeline to require minimal human intervention so that it can work in massively distributed settings.

We generalize to the following conditions:

(1) as low as only one image per facade;
(2) possibly more than one facade in an image (see 3.2);
(3) arbitrary aspect ratio and resolution;
(4) arbitrary viewing angle, and no apriori knowledge of viewing angle or relevant camera parameters (see 3.3);
(5) facade occlusions (see 3.4);
(6) grayscale;

These constraints significantly limit the amount of prior knowledge we can bring to bear in Nostalgin, making the underlying reconstruction task far more difficult and preventing usage of most prior work. However, these assumptions allow us to generalize to Nostalgin to real historical image data in a massively scalable way.

Our pipeline makes the following assumptions:

(1) the facades come from a Manhattan-world environment[1];
(2) images are weakly geotagged such that we are given the relative position of where each image was taken with respect to neighboring images (see 3.5);
(3) the width for each facade is known relative to other facades.

3.2 Image Parsing

In order to gain insight from an image, we must first identify what objects are in the image and where they are actually located in

[1]A Manhattan-world assumption is the assumption that most buildings are relatively planar and lie on a cartesian grid, as in Manhattan. For example, we do not expect our pipeline to accurately handle domes.

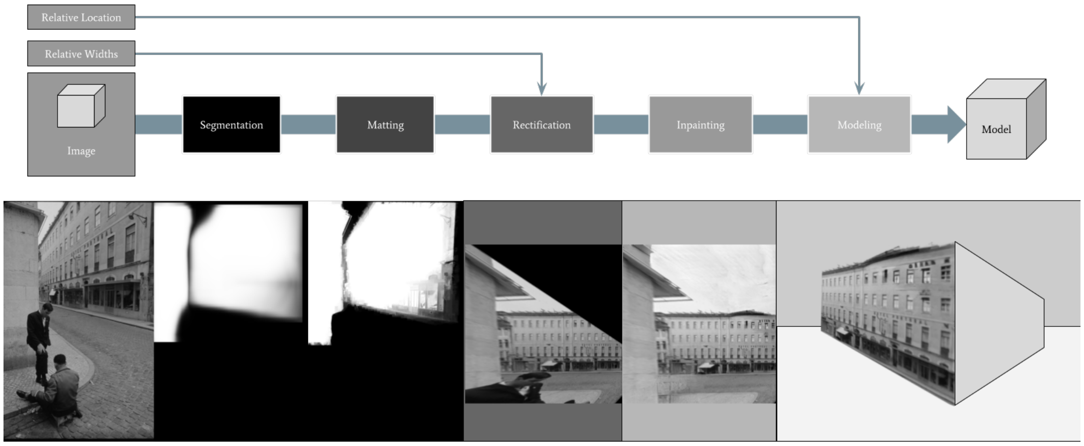

Figure 2: Components in our modeling pipeline.

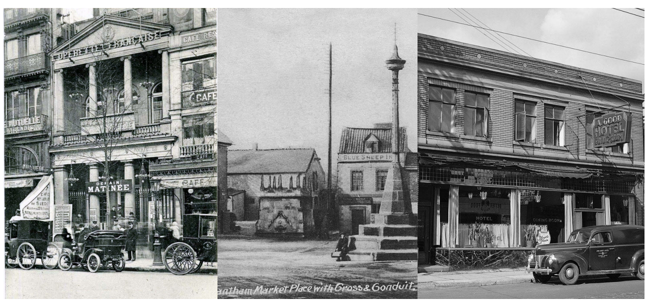

Figure 3: Examples of real world image data.

pixel space. This includes identifying key objects of interest, such as one or many building facades, as well as identifying occlusions that may be blocking the full building image. Any kind of parsing should produce sharp boundaries around the parsed object in order to provide shape information to later components and to ensure that no pixel information is lost.

Deep neural network models have made incredible strides in image segmentation and classification tasks. Thus, for our pipeline, we utilize the popular MaskRCNN deep neural network architecture [8]. We detect two classes of objects: building facades, and occlusions. In particular, we aim to label people and cars as occlusions. The MaskRCNN model is pretrained on COCO and fine tuned on a set of roughly 30k images that are manually labelled with masks around facades. A well known problem with this class of neural segmentation models is that the model struggles with providing extremely tight image boundaries. In order to address this issue, we add an image-gradient-based postprocessing step known as alpha matting [16]. Alpha matting significantly improves the contours of our masks. Further analysis of the addition of alpha matting can be found in Section 4.1.

3.3 Viewpoint Normalization

The second task within our pipeline is to normalize the image with respect to camera viewpoint. This normalization takes the form of rectifying facades defined by a set of masks in an image. The goal of this normalization is to simplify downstream tasks to make it easier to extract depth and infer missing contextual information. Because we lack camera parameters and use real world images with many confounding objects in the scene, we develop our own rectification method based on previous work.

3.3.1 Low-Signal Line Detection. Almost all rectification approaches rely on accurate line detection in an image. Real world data often has complex structures that make line extraction difficult. Historical images additionally suffer from poor resolution, scanning artifacts, and image damage. As a result, we are unable to use off-the-shelf line detection methods such as the Probabilistic Hough Transform. Instead, we devise our own line detection algorithm that preserves lines that are good candidates for vanishing point detection and removes other lines. We provide brief analysis of other line detection methods in 4.2.1.

In order to capture as much signal as possible, we first run Canny edge detection with full connectivity and dynamically compute the thresholds given image median $\tilde{x}$ and hyperparameter $\lambda \in (0, 1)$ as follows.

$$l = \max(0, \tilde{x}(1 - \lambda)) \quad \text{and} \quad u = \min(255, \tilde{x}(1 + \lambda)) \tag{1}$$

where λ represents the tightness of our Canny thresholds. We then join all continuous points into contours.

To detect facade position, we want our line detector to only preserve straight lines. For each contour, we label every point as "linear" or "non-linear" by computing the second discrete derivative. Once labeled, non-linear points are removed and all remaining points are re-linked into new contours. We define the angle at a single point p along the contour C as

$$\alpha(C, p) = arctan\left(\frac{\mathrm{d}p}{\mathrm{d}C}\right) \tag{2}$$

Using this, we define the left-hand second derivative as

$$L_\alpha(C, p) = \frac{1}{k_s} \sum_{d=1}^{k_s} ||\alpha(C, p) - \alpha(C, p - d)||_\theta \tag{3}$$

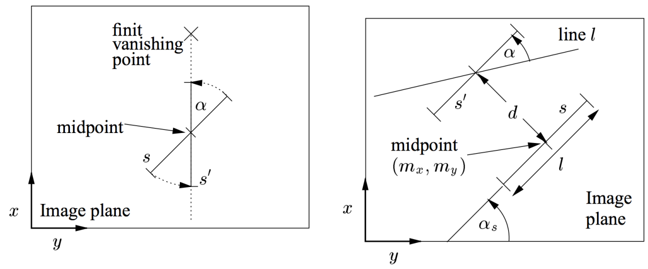

(a) **Explanation for the distance function $d(vp, s) = \alpha$ between a line segment s and a finite vanishing point vp.**

(b) **Explanation for the distance function $d(l, s)$ between infinite vanishing point l and segment s.**

Figure 4: Duplicated from [21]: distance functions used to determine fit between a line segment and an (in)finite vanishing point.

and the right-hand second derivative as

$$R_\alpha(C, p) = \frac{1}{k_s} \sum_{d=1}^{k_s} ||\alpha(C, p) - \alpha(C, p + d)||_\theta \tag{4}$$

where $||\theta_1 - \theta_2||_\theta$ is the measure of the smallest angle between θ_1 and θ_2, and where k_s is the window size of the discrete derivative. Using Equations 3 and 4 and given a linearity threshold for the second derivative t_α, we label each point along a contour and fit line segments to each locally-linear sub-contour using RANSAC [6]. The algorithm for defining local linearity is provided in the Appendix.

3.3.2 Vanishing Point Detection. Vanishing point detection helps convert lines into depth information. Detecting vanishing points is a task traditionally solved in two steps: first, detected line segments are used to accumulate a list of potential vanishing point candidates; and second, the segments are used to rank the candidates.

During accumulation, we reduce the candidate search space by deduplicating collinear line segments and vanishing point candidates using quantization within our error bounds (see 4.2.2). During voting, we modify Rother's voting function such that the resulting weights correspond to the percent of evidence accounted for by the vanishing point[2]. Thus, we define that for a candidate vanishing point a, set of line segments S, facade mask m, and alignment threshold t_a

$$vote(a, S, m) = \frac{\sum_s^S \left[||s||_2 \omega(s, m)(1 - \frac{d(a,s)}{t_a})\right]}{\sum_s^S \left[||s||_2 \omega(s, m)\right]} \tag{5}$$

where $\omega(s, m)$ is a weighting function defined as the count of pixels on segment s within mask m normalized by the length of segment s. This is done to ensure that only pixels within a facade mask vote towards vanishing points for that facade. Note that function $d(a, s)$, shown in Figure 4, is taken directly from [21]. Also, note that the alignment threshold t_a measures the maximum distance $d(a, s)$ between a vanishing point and line segment that still constitutes alignment.

[2]For example, a value of 1.0 indicates a perfect match with all segments, whereas a value of 0.5 indicates that roughly half of segments match.

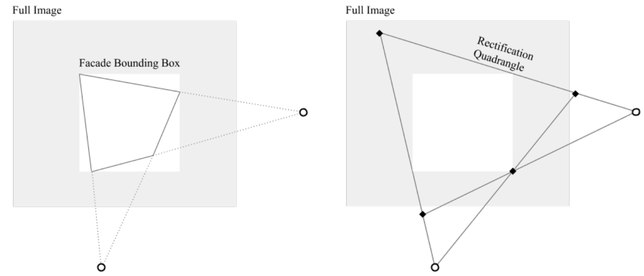

(a) Vanishing points and facade. **(b) The rectification quadrangle.**

Figure 5: Computation of the facade bounding-quadrangle.

We select the most highly weighted vanishing point as scored using the corresponding facade mask m, and the second most highly weighted vanishing point that is at least t_o degrees offset from the first, to find two vanishing points representing facade orthogonal lines.

3.3.3 Quadrangle Estimation. Once two vanishing points have been chosen, forming a vanishing point aware minimum-bounding quadrangle – i.e. the smallest quadrangle that adheres to the facade's two vanishing points and also includes all of the facade's masked pixels – is relatively straight-forward. Given the facade's pixel-mask, we can readily compute the bounding box for the facade. From this, we project lines from each vanishing point to the nearest corners of the bounding box and form a quadrangle from the four intersections created (see Figure 5). The resulting quadrangle is a representation of the facade-plane projected onto the image-plane and resized to contain all masked facade-pixels.

3.3.4 Rectification. In order to finish the rectification of the facade in the image, we need to predict the aspect ratio of the final image. Many existing approaches are able to leverage known camera parameters; however, working with general historical data naturally precludes any reliance on such information. Instead, we predict that the camera's principal point is the center of the image and that there is no skew in the image. This requires us to estimate only the focal length, which can be approximated using vanishing point geometry. We note that this can result in some error, but qualitative results suggest that the visual impact of imperfect focal length prediction is minimal within certain reasonable error bounds.

With a single quadrangle per-facade and an approximate focal distance, we can directly apply [28] to determine the aspect ratio of the resulting rectified image. The aspect ratio and quadrangle vertices together give four corresponding points between the facade-plane and the rectification-plane which are sufficient to compute a rectification homography. This allows us to manipulate the facade in the image such that it looks like the camera pose has shifted to the front of the facade. Once we have the rectified facade and the appropriate aspect ratio, we use the given width of the facade image to scale the facade relative to its real world location context.

3.4 Occlusion Removal

The third task is to normalize the image with respect to occlusions. This component also ingests a set of masks and an image, and outputs an inpainted image with the inpainting occurring in the masked locations. Importantly, any approach used for inpainting had to handle fairly high-resolution images (larger than 800 x 800 pixels) and had to work for large, arbitrary masks.

3.4.1 Inpainting Methods. We examine several deep and algorithmic approaches, and describe our analysis in Section 4.3. We build on the Free Form inpainter suggested by [26]. Specifically, we create a two-stage conditional fully-convolutional GAN with an SNPatch Discriminator, trained on black and white images.

The Free Form approach is memory intensive for images larger than 250x250 pixels. In order to solve this issue, we decrease the width of the model by nearly 25% and double the stride of the contextual attention layer. We also develop a 'Low Memory' Inpainter that takes an input image and a set of masks, splits the image to only include the mask and a small surrounding area based on a preset context radius, and inpaints each split separately. These approaches to decreasing memory usage also decrease accuracy. We discuss these tradeoffs in 4.3.2.

3.4.2 Dataset. A convenient aspect of the Free Form method is that it learns how content extends across 2D geometry instead of learning to represent a specific object class. This is especially important in historical settings, where it is difficult to collect a large dataset of a specific object. We collect a dataset of 10M modern and historical images. We require only that each image has at least one facade in the image. We convert each image to black and white, and train the model on 600x400px random crops. We refer to this dataset as the 10M dataset.

3.5 Modeling

The final task is to generate a 3D city model. This component expects a set of cropped facade images that are to-scale, each with relative location information. For this work, we assume that the buildings will appear in a grid-like city block formation; as such, the model only requires the left- or right-side neighbors of each facade, whether two facades come from the same building, and the location of each block relative to each other.

We utilize the facade location data to create a chain of facades that wrap around each block, and then place the blocks relative to each other. For each facade, we create a cuboid 3D model with matching proportions; if more than one facade is given for the same building, we can exactly specify the parameters of the cuboid model. We provide the algorithm for placing buildings within a block in the Appendix. The complete algorithm for placing blocks is a trivial extension.

For each cuboid model, we apply the relevant input facade images as textures. If four facades are not given, we tile the given facades around all four sides of the cuboid. We make all parts of the image that are not part of the facade transparent before texture application, utilizing matting masks to determine where facade boundaries are.

4 EXPERIMENTS

In this section we motivate specific design decisions through qualitative and quantitative measures of performance for each subcomponent in the larger 3D modeling pipeline. For all experiments, see the Appendix for additional details on hyperparameter settings, evaluation datasets, loss calculations, and more.

Table 1: Quantitative Segmentation Comparison

	Precision	Recall	$l1$	$l2$
MaskRCNN	86.1 ± 10.3	78.2 ± 5.3	10.9 ± 8.1	8.2 ± 7.9
Matting	75.2 ± 13.1	86.5 ± 8.2	10.4 ± 8.5	7.6 ± 7.3

Figure 6: Qualitative analysis of matting improvements to segmentation. From left to right, we show the input image with the manually labeled ground truth, the MaskRCNN output, the generated trimap, and the output of alpha matting. Best viewed with zoom.

4.1 Segmentation and Matting

For image segmentation, we utilize a MaskRCNN architecture. MaskRCNN is one of the most popular image segmentation architectures due to its ease of implementation and effectiveness in applied settings. We train the MaskRCNN model to select facades and occlusions (people, cars) in images[3]. However, we find that MaskRCNN masks degrade close to segmentation boundaries. This results in significant decrease of quality in later parts of the pipeline.

In order to produce tighter image boundaries, we examine image matting algorithms. We convert the output MaskRCNN model to a trimap, using the probabilities of the MaskRCNN to map the range of 5% to 95% as uncertain. We then apply the image gradient-based alpha matting algorithm from [16]. Using manually labeled ground truth masks, we compare precision, recall, $l1$ loss, and $l2$ loss in Table 1. We show qualitative results in Figure 6 and quantitative results in Table 1.

We find that the masks produced by matting capture boundaries *better* than the manually labeled ground truth around difficult edges that manual labelling ignored. We also note that because we did not explicitly capture every facade in every image, images where the MaskRCNN missed a facade or captured one that was not in ground truth caused large variations in quantitative metrics. This explains a significant amount of the error and variance in both precision and recall.

[3]We note that it is easy to train for more classes of occlusions; for this proof of concept work, we selected the two most common occlusion types.

(a) LSD **(b) Hough Transform** **(c) Nostalgin**

Figure 7: Qualitative analysis of line-detection methods. Best viewed with zoom.

Table 2: % Reduction of Vanishing Point Candidates

	Search Space	Wall Time
Deduplicate Collinear Segments	41.0 ± 16.1	33.1 ± 29.8
Deduplicate Infinite VPs	11.4 ± 19.1	10.1 ± 7.5
Combined	**44.3 ± 18.7**	**35.6 ± 37.7**

4.2 Rectification

4.2.1 Analysis of Line Detection Methods. Traditional approaches for line detection such as Probabilistic Hough Transform or LSD [23] are attractive because they require no hyperparameter tuning and can be applied with little-to-no development cost using tools such as OpenCV. However, we observe that these line detectors yield poor rectifications, as occlusions such as people, tree, and cars in addition to building ornamentation such as domes, arches, and statues dilute the signal of the facade. Specifically, off-the-shelf line detectors end up accommodating 'curvy' occlusions by segmenting each contour into countless little lines at varying angles.

Our proposed method strengthens the signal of the facades and removes line data coming from ornamentation and occlusions. See Figure 7 for a qualitative comparison of the proposed methods and traditional approaches. We note that ornamentation along the roof and the occluding statue are less represented when using our proposed method. This allows our pipeline to focus on lines that actually provide depth information about the plane of the facade.

4.2.2 Vanishing Point Space Reduction. In our initial rectification implementation, we noticed that the process of selecting, accumulating, and voting on appropriate vanishing points was responsible for over half of our run-time. We recognized that many of the vanishing points that were being analyzed were duplicates or near duplicates. We took efforts to decrease the vanishing point analysis space by reducing colinear line segments and infinite vanishing point segments. We measure the percent reduction of the search space and the wall time in Table 2.

4.3 Inpainting

4.3.1 Analysis of Inpainting Methods. We examine several traditional and deep learning approaches to inpainting. As far as we are aware, there are no industry standard methods of quantifying the quality of an inpainted image. In this work, we follow [26] and use mean $l1$ and $l2$ loss as quantitative metrics. We note that these metrics have tenuous relation to the visual outcome of inpainting, especially when the inpainter is purposely attempting to remove an object or objects from a scene; thus, we rely heavily on qualitative results.

Table 3: Inpainting Quantitative Comparison

	Per Pixel l_1 Loss	Per Pixel l_2 Loss
PatchMatch*	11.3	2.4
Global&Local*	21.6	7.1
ContextAttention*	17.2	4.7
PartialConv*	10.4	1.9
FreeForm*	9.1	1.6
Nostalgin	9.8 ± 4.2	2.5 ± 4.2
Nostalgin (Low Memory)	10.4 ± 4.1	2.8 ± 1.8

Loss values for starred methods taken from [26].

Traditional approaches to inpainting are promising because they require minimum or no training time and can handle large images with relatively small increases in memory cost (though often with a very large increase in computation time). Such approaches rely on local similarity metrics that allow semi-accurate 'copy paste' operations. Diffusion based methods such as the Navier Stokes method [4] propagate immediate neighboring pixel information based on image gradient information; while patch based methods such as PatchMatch [3] extend groups of local pixels based on low level features. These methods are powerful, but scale poorly to larger masks both in terms of quality and run-time.

In contrast, deep approaches to inpainting are promising because they learn semantic features across an entire image. Further, the run-time for deep approaches is often not a function of mask size. Several deep approaches, such as Semantic Inpainting [24], are not resolution independent. These models require train and inference image sizes to be the same due to the presence of non-convolutional layers in the model. Other deep approaches such as Inpainting with Contextual Attention [27] are dependent on specific a mask shape and location and do not generalize well to arbitrary masks.

The Free Form method proposed in [26] fulfills our requirements, and we adapt it for this work. We discuss methods to improve the scalability of this approach in 4.3.2; we decide to decrease model capacity in exchange for better run-time. In Figure 8 and Table 3 we respectively provide qualitative and quantitative analysis of several of the mentioned methods.

4.3.2 Inpainter Scalability. Though the Free Form model has better accuracy at higher resolutions than other tested methods, it is fairly memory and compute intensive when trained on high-resolution images (600x600) and used for inference on very high-resolution images (1200x1200). In this section we describe methods of decreasing the memory and computational load.

Given an image size, the two hyperparameters that have the biggest impact on computational cost are the base layer width (all layers in the model are a multiple of this hyperparameter) and the stride of the contextual attention layer. Both of these hyperparameters relate to model capacity; reducing capacity likely impacts the quality of the inpainting model. To examine this relationship, we

(a) Original Image and Input Mask

(b) PatchMatch **(c) Free Form**

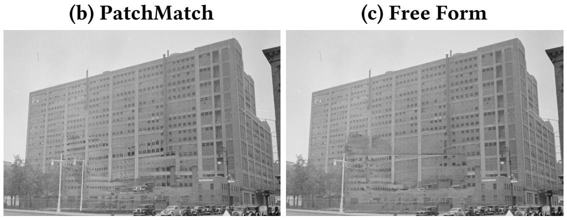

(d) Nostalgin **(e) Nostalgin (Low Memory)**

Figure 8: Qualitative analysis of inpainting methods. Best viewed with zoom. Image courtesy of the New York Municipal Archives.

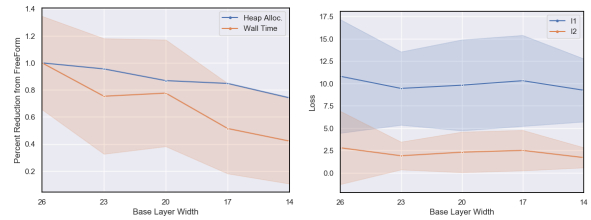

(a) Base Layer Width

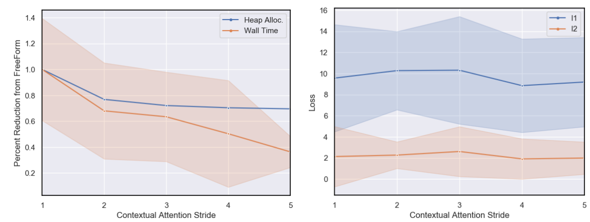

(b) Contextual Attention Stride

Figure 9: Measurement of scalability and loss metrics over changing hyperparameters.

separately vary these two hyperparameters and measure the quantitative loss scores and run-time metrics in Figure 9. As expected, decreasing the base layer width results in less heap allocation and less wall time usage, as there are less parameters in the model. Increasing the stride of the contextual attention layer has a similar effect, although we note that the decrease in allocated memory levels off. We expected $l1$ and $l2$ loss to increase as model capacity decreases. Instead, we observe a slight trend in the *opposite* direction. We note that there are extremely high standard deviations, making it difficult to draw meaningful conclusions from the loss metrics. In accordance with our original hypothesis, we observe significant visual degradation in qualitative tasks when using hyperparameter settings that result in decreased model capacity, despite similar loss values. We believe this further suggests that $l1$ and $l2$ loss have a low correlation to inpainting quality. Based on our overall observations and our run-time measurements, we select a base layer width of 20 and a contextual attention stride of two[4].

Inpainting images larger than 1200x1200px is challenging even with decreased model size. To solve this, we slice the image around each separated mask component and inpaint each slice separately. We then stitch the results back together. We call this approach 'Low Memory' Inpainting. We analyze the percent reduction in memory and in run-time in Table 4. Here, 'Nostalgin' refers to a Free Form inpainting model with the hyperparameter changes discussed above. Note that we do not report the standard deviation for heap allocation; to calculate heap allocation, we could only easily measure the final heap across our evaluation set. We divide that value by the number of evaluation images.

[4]Compared to baseline values of 26 and one respectively.

Table 4: % Reduction in Inpainting Scalability Metrics

	Wall Time	Heap Alloc.
Nostalgin (Full Image)	54.7 ± 4.6	27.8
Nostalgin (Low Memory)	90.7 ± 3.1	79.6

All percentages compared to the FreeForm method [26].

4.4 Modeling

We examine the 3D modeling pipeline end to end by utilizing a set of facade image data to reconstruct two blocks of Manhattan as it looked in the 1940s. The image data for these two blocks are taken from a tax record collection maintained by the New York Municipal Archives. Figure 10 depicts an input image as it goes through the 2D processing components described above, and demonstrates how clean facades can be extracted. Specifically, we are able to extract two rectified and inpainted facades from a single black and white image of a corner building.

We are able to run this pipeline at scale for many images in a distributed fashion. We demonstrate this in Figure 11, which depicts several angles of our generated city blocks (additional images in the Appendix). We note that the generated environment is fully walkable; the images presented in the figure are screenshots of a larger simulation instead of one-off renderings. Thus, we are able to easily generate viewing angles that are not present in the initial images, showing the power of our approach. We also compare our reconstruction to modern day images taken from Google Streetview. We highlight that several buildings have changed significantly or have completely been removed; as a result, our 3D reconstruction is capable of capturing an experience that no longer exists.

(a) Input. (b) Segment Facade, Occlusions.

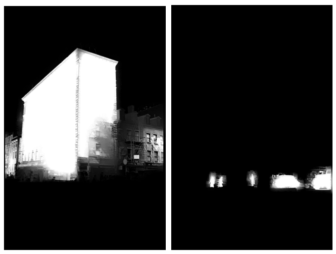

(c) Mat Facade, Occlusions.

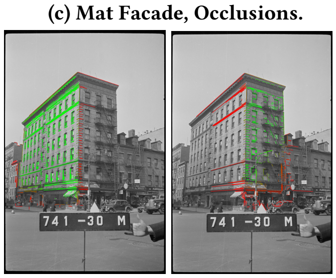

(d) Extract Lines.

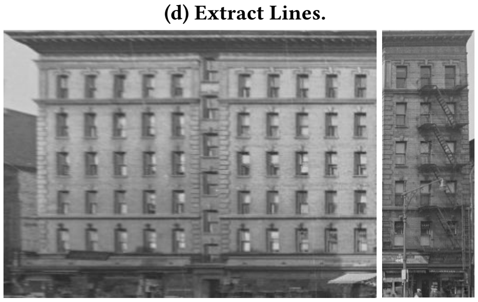

(e) Final Results (Rectify, Inpaint).

Figure 10: End to end processing pipeline depicting 2D facade extraction, rectification, and inpainting. Input image courtesy of New York City Municipal Archives.

(a) 7th Ave, 17th St, NW Corner.

(b) 9th Ave, 17th St, SE Corner.

(c) 9th Ave, 18th St, SW Corner.

Figure 11: Qualitative analysis of inpainting methods. From left to right, we show the original image data (courtesy of the New York City Municipal Archives), our 3D reconstruction, and the modern day (taken from Google Streetview). All images are from New York, NY.

5 CONCLUSION AND FUTURE WORK

Automatic city reconstruction from historical images is a difficult task because historical images provide few guarantees about image quality or content and often do not have important metadata required to extract 3D geometry. In this work, we propose and motivate Nostalgin, a scalable 3D city generator that is specifically built for processing high-resolution historical image data. We describe a four part pipeline composed of image parsing, rectification, inpainting, and modeling. For each component, we examine several design choices and present quantitative and qualitative results. We show that each subcomponent is built to uniquely handle the inherent difficulties that arise when dealing with historical image data, such as sparsity of images and lack of metadata. We demonstrate the end-to-end pipeline by reconstructing two Manhattan city blocks from the 1940s.

We aim to leverage the power of Nostalgin to create an open source platform where users can contribute their own photos and generate immersive historical experiences that will allow them to connect to prior eras of history. Additional data collected from such a platform would help us further generalize Nostalgin, helping us move towards full 3D reconstruction of all types of buildings. We also are beginning to examine how we can extract geolocation information from historical plot data, allowing us to move away from any geotagging requirements.

We believe Nostalgin enables users to experience historical settings in a way that was previously impossible. We are excited for future developments in the historical 3D city modeling space.

ACKNOWLEDGMENTS

We would like to acknowledge Noah Snavely; without his guidance, this work may not have been done. We would also like to acknowledge Bryan Perozzi, Vahab Mirrokni, Feng Han, and Ameesh Makadia. Finally, we would like to thank the New York City Municipal Archives for their support.

REFERENCES

[1] Sameer Agarwal, Noah Snavely, Steven M Seitz, and Richard Szeliski. 2010. Bundle adjustment in the large. In *European conference on computer vision*. Springer, 29–42.

[2] Sameer Agarwal, Noah Snavely, Ian Simon, Steven M Seitz, and Richard Szeliski. 2009. Building rome in a day. In *Computer Vision, 2009 IEEE 12th International Conference on*. IEEE, 72–79.

[3] Connelly Barnes, Eli Shechtman, Adam Finkelstein, and Dan B Goldman. 2009. PatchMatch: A randomized correspondence algorithm for structural image editing. *ACM Transactions on Graphics (ToG)* 28, 3 (2009), 24.

[4] Marcelo Bertalmio, Andrea L Bertozzi, and Guillermo Sapiro. 2001. Navier-stokes, fluid dynamics, and image and video inpainting. In *Computer Vision and Pattern Recognition, 2001. CVPR 2001. Proceedings of the 2001 IEEE Computer Society Conference on*, Vol. 1. IEEE, I–I.

[5] Angel X Chang, Thomas Funkhouser, Leonidas Guibas, Pat Hanrahan, Qixing Huang, Zimo Li, Silvio Savarese, Manolis Savva, Shuran Song, Hao Su, et al. 2015. Shapenet: An information-rich 3d model repository. *arXiv preprint arXiv:1512.03012* (2015).

[6] Martin A. Fischler and Robert C. Bolles. 1981. Random Sample Consensus: A Paradigm for Model Fitting with Applications to Image Analysis and Automated Cartography. *Commun. ACM* 24, 6 (June 1981), 381–395. https://doi.org/10.1145/358669.358692

[7] Kota Hara, Raviteja Vemulapalli, and Rama Chellappa. 2017. Designing deep convolutional neural networks for continuous object orientation estimation. *arXiv preprint arXiv:1702.01499* (2017).

[8] Kaiming He, Georgia Gkioxari, Piotr DollÃąr, and Ross Girshick. 2017. Mask R-CNN. *arXiv:1703.06870* (2017).

[9] Youichi Horry, Ken-Ichi Anjyo, and Kiyoshi Arai. 1997. Tour into the picture: using a spidery mesh interface to make animation from a single image. In *Proceedings of the 24th annual conference on Computer graphics and interactive techniques*. ACM Press/Addison-Wesley Publishing Co., 225–232.

[10] Arnold Irschara, Christopher Zach, and Horst Bischof. 2007. Towards wiki-based dense city modeling. In *Computer Vision, 2007. ICCV 2007. IEEE 11th International Conference on*. IEEE, 1–8.

[11] Nianjuan Jiang, Ping Tan, and Loong-Fah Cheong. 2009. Symmetric architecture modeling with a single image. *ACM Transactions on Graphics (TOG)* 28, 5 (2009), 113.

[12] Tom Kelly, John Femiani, Peter Wonka, and Niloy J Mitra. 2017. BigSUR: large-scale structured urban reconstruction. *ACM Transactions on Graphics (TOG)* 36, 6 (2017), 204.

[13] Thommen Korah, Swarup Medasani, and Yuri Owechko. 2011. Strip histogram grid for efficient lidar segmentation from urban environments. In *Computer Vision and Pattern Recognition Workshops (CVPRW), 2011 IEEE Computer Society Conference on*. IEEE, 74–81.

[14] Jana Košecká and Wei Zhang. 2002. Video compass. In *European conference on computer vision*. Springer, 476–490.

[15] Jana Košecká and Wei Zhang. 2005. Extraction, matching, and pose recovery based on dominant rectangular structures. *Computer Vision and Image Understanding* 100, 3 (2005), 274–293.

[16] Anat Levin, Dani Lischinski, and Yair Weiss. 2008. A Closed Form Solution to Natural Image Matting. *IEEE Transactions on Pattern Analysis and Machine Intelligence* 30, 2 (2008), 228–242.

[17] Hantang Liu, Jialiang Zhang, Jianke Zhu, and Steven CH Hoi. 2017. Deepfacade: A deep learning approach to facade parsing. (2017).

[18] Przemyslaw Musialski, Peter Wonka, Daniel G Aliaga, Michael Wimmer, Luc Van Gool, and Werner Purgathofer. 2013. A survey of urban reconstruction. In *Computer graphics forum*, Vol. 32. Wiley Online Library, 146–177.

[19] Gen Nishida, Adrien Bousseau, and Daniel G Aliaga. 2018. Procedural Modeling of a Building from a Single Image. In *Computer Graphics Forum*, Vol. 37. Wiley Online Library, 415–429.

[20] Byong Mok Oh, Max Chen, Julie Dorsey, and Frédo Durand. 2001. Image-based modeling and photo editing. In *Proceedings of the 28th annual conference on Computer graphics and interactive techniques*. ACM, 433–442.

[21] Carsten Rother. 2002. A new approach to vanishing point detection in architectural environments. *Image and Vision Computing* 20, 9–10 (2002), 647–655.

[22] Carlos A Vanegas, Daniel G Aliaga, Peter Wonka, Pascal Müller, Paul Waddell, and Benjamin Watson. 2010. Modelling the appearance and behaviour of urban spaces. In *Computer Graphics Forum*, Vol. 29. Wiley Online Library, 25–42.

[23] Rafael Grompone von Gioi, Jeremie Jakubowicz, Jean-Michel Morel, and Gregory Randall. 2010. LSD: A Fast Line Segment Detector with a False Detection Control. *IEEE Transactions on Pattern Analysis and Machine Intelligence* 32, 4 (2010), 722–732.

[24] Raymond A Yeh, Chen Chen, Teck Yian Lim, Alexander G Schwing, Mark Hasegawa-Johnson, and Minh N Do. 2017. Semantic image inpainting with deep generative models. In *Proceedings of the IEEE Conference on Computer Vision and Pattern Recognition*. 5485–5493.

[25] Xuetao Yin, Peter Wonka, and Anshuman Razdan. 2009. Generating 3d building models from architectural drawings: A survey. *IEEE computer graphics and applications* 29, 1 (2009).

[26] Jiahui Yu, Zhe Lin, Jimei Yang, Xiaohui Shen, Xin Lu, and Thomas S Huang. 2018. Free-Form Image Inpainting with Gated Convolution. *arXiv preprint arXiv:1806.03589* (2018).

[27] Jiahui Yu, Zhe Lin, Jimei Yang, Xiaohui Shen, Xin Lu, and Thomas S Huang. 2018. Generative image inpainting with contextual attention. *arXiv preprint* (2018).

[28] Zhengyou Zhang. [n. d.]. Single-View Geometry of A Rectangle With Application to Whiteboard Image Rectification.